Nuclear Instruments and Methods in Physics Research A 1062 (2024) 169196

Contents lists available at ScienceDirect

Nuclear Inst. and Methods in Physics Research, A

journal homepage: www.elsevier.com/locate/nima

Full Length Article

Approaching an optimum time resolution for synchroscan streak-camera measurements with visible synchrotron light

G. Schiwietz *, M. Koopmans, Ch. Kalus, M. Marongiu, A. Schälicke, P. Schnizer, M. Ries

Helmholtz-Zentrum Berlin für Materialien und Energie GmbH, Albert-Einstein-Str. 15, Berlin, 12489, Germany

ARTICLE INFO

Keywords:
Electron-beam diagnostics
High-resolution streak-camera system
Non-destructive bunch-length measurements
Bunch-selectivity

ABSTRACT

The optical beam diagnostics at the BESSY II light source in Berlin have been improved significantly over the last few years. In particular, the streak-camera system has been extended in precision and sensitivity to allow two-dimensional imaging in time and space for equilibrated and non-equilibrated bunch patterns. In this paper, we prove experimentally and theoretically that we have reached a sub-ps RMS total time resolution using filtered synchrotron light. Detailed simulations, including the different physical time-dispersion mechanisms, show the influence of various band-pass and edge wavelength filters on the resolution. The limits for unfiltered near-visible synchrotron radiation (white-light) and the band-pass filter to achieve optimal time resolution are derived as well, providing a basis for more advanced beam-dynamics studies in the near future.

1. Introduction

Charged-particle diagnostics is important for the commissioning of accelerator complexes, for feedback and feed forward tasks, as well as for quality control and machine protection. In principle, electron-beam diagnostics of pulsed beam structures tries to provide quantitative data, on the total particle-beam current, the radiation in the surrounding of beam pipes for the detection of beam losses with high sensitivity, on the position of the beam, the size or even on the shape of the beam in both transverse directions, on the timing pattern of populated buckets and on the current or integrated charge of each bunch, on a time-shift of each bunch (phase) with respect to a reference clock, and on the bunch length or even on the shape of the beam in the longitudinal direction.

For most of the above quantities, there is a large variety of experimental methods that may be applied. Regarding the transverse quantities, we refer the reader to the review by G. Kube [1] on transversal diagnostics methods. Other key issues in electron-beam diagnostics is the measurement of the bunch length, the bunch phase or even the full temporal (longitudinal) distribution. An overview over many different bunch-length measurement techniques has been presented by T. Lefevre [2].

The available diagnostic methods can be classified according to their potential to keep the bunch structure more or less undisturbed during the measurement: there are destructive methods [3,4], partially destructive [5–11], and non-invasive methods [12–16].

Probably the most common method for longitudinal beam-profile diagnostics is the application of a fast streak camera (FSC) in the visible-light regime. The review by K.Scheidt [16] is suggested as a compact introduction into the corresponding techniques, and the application for free-electron-laser diagnostics has been discussed by A.H.Lumpkin [17] (further details may also be extracted from related PhD theses [18,19]).

The use and characterization of an FSC will be discussed throughout this paper. Typically, synchroscan systems may achieve an accurate (sub-ps) time stability and, for short laser pulses at a long wavelength, they reach optimum time resolutions between 0.4 and 1.3 ps RMS. Here we will focus on the tradeoff between accumulated light intensity, wavelength spectrum, data-acquisition time and best optimal time resolution by combining various experimental data and simulations that consider three different wavelength-dependent sources of time dispersion for synchrotron light analyzed with a streak camera. We will show that single-shot FSC images (single-turn acquisition) have been obtained at a resolution of about 1.3 ps RMS with our FSC [19] and we prove that an optimized synchroscan system may yield a minimum time resolution below 0.5 ps RMS under realistic operating conditions. With this resolution, advanced beam-dynamics investigations of arrival time (phase), bunch length as well as even temporal bunch shape will be possible [20].

2. BESSY II

The present BESSY II electron-storage ring of Helmholtz-Zentrum Berlin (HZB) is operated at an electron energy of 1.7 GeV with an RF

* Corresponding author.
E-mail address: g.schiwi@t-online.de (G. Schiwietz).

https://doi.org/10.1016/j.nima.2024.169196
Received 1 January 2024; Received in revised form 15 February 2024; Accepted 21 February 2024
Available online 23 February 2024

Table 1
Main parameters of BESSY II in standard mode operation.

Parameter	Value
Beam energy (GeV)	1.7
Beam current (mA)	300
RMS bunch-length (ps)	20
Bunch separation (ns)	2
Number of buckets	400
RF frequency (MHz)	500
Bending magnet field (T)	1.3

cavity frequency of 500 MHz. The typical beam current is 300 mA in top-up operation; in Table 1 the relevant parameters for this paper are shown. Different operation modes are available and various complex filling patterns [21] can be applied to within 400 RF buckets separated by approximately 2 ns. Beam loading as well as possible bunch-to-bunch interactions call for selective diagnostics of individual bunches by either taking single-turn images or averaging over many revolutions. In particular, it is the aim of this work to prepare for detailed beam-dynamics investigations at the short pulse limit of our storage ring.

One method of achieving sub-picosecond bunch lengths (τ) is the reduction of the momentum compaction factor (α) towards an isochronous lattice. The momentum compaction factor is defined by $\frac{\delta L}{L} = \alpha \frac{\delta p}{p}$, where L is the total path length of a particle orbit around the ring and p is the corresponding reference momentum. For very small α, it is relevant to take higher orders of $\frac{\delta p}{p}$ into account to preserve the momentum acceptance [22]. For this purpose, we have set up a dedicated sextupole setting in negative low-α mode ($\alpha < 0$). This mode allows for operating conditions when α is reduced from its standard value of about 7×10^{-4} to values below 1×10^{-5} at small bunch currents and high cavity voltages of 2 MV [15,23]. During the different experimental runs presented in Section 5, the nominal synchrotron oscillation frequency was $f_{sync} \approx 400$ Hz (measured using a diagnostics stripline) and the bunch currents were around $I_{bunch} \approx 0.85\,\mu$A; the filling pattern was stable at a beam lifetime exceeding 40 h, giving us enough time to take various streak-camera images.

Relying on the relation $\tau \propto \sqrt{|\alpha|} \propto f_{sync}$ between bunch length τ and the dipole mode of the synchrotron oscillation in the zero-current approximation, one may estimate an RMS bunch-length slightly below 1 ps. This is in accordance with bunch lengths determined previously from THz spectra under similar conditions [15].

2.1. Beamline setup

The optical timing beamline (Dip.1.1 at sector L12) for the streak camera has been described in detail recently [19,24] and is shown schematically in Fig. 1. Measurements with a fast streak camera as well as interferometry of the vertical beam size [19] by using the X-ray baffle method with π-polarized visible light [25,26] are possible at this diagnostic beamline. The vacuum part of the beamline is completely motor controlled.

The light path starts with the bending magnet BM2T6R, followed by an X-ray blocking baffle to avoid excessive heat loads on the subsequent two custom-made mirrors. These are a cooled large ellipsoidal focusing mirror (manufactured by Carl Zeiss Laser Optics GmbH, Germany) producing an intermediate point focus and a toroidal mirror (custom product manufactured by WinlightX, France) for beam collimation. The light beam resulting from the corresponding large source-opening angle of about 20 mrad horizontally and 3.5 mrad vertically (open-area values, considering the vertical extension of the first mirror and of the X-ray blocking baffle) leads to a beam power of about 5.5 mW in the near-visible range at standard user-beam conditions and good focusing properties.

In contrast to our standard streak-camera setup [24], for the current experiment we have removed the polarizer as well as all the intermediate beam splitters, and we have added a wedge-compensation window (3 mm fused silica, with the wedge direction rotated by 180°) for counteracting the position dispersion due to the wedged exit window that would otherwise develop along the final light path of about 5 m to the FSC. Overall, the above changes are minimizing dispersion effects and maximizing the light intensity at the focusing lens (an achromatic doublet) in front of the streak-camera entrance. Two filter wheels have been used on the optical table for changing between white-light illumination and optical band-pass, as well as high-pass edge filters at different wavelengths λ_{cut}. Eight high quality plane mirrors (surface flatness $\lambda/20$) and several collimators in the light-transport system give rise to a good signal-to-noise ratio in the streak-camera images that lead to a dynamic range of 1 to 2000 for the bunch intensities.

The optical beamline was set to the so-called t/x mode by sending the light to the optical table via both mirrors "M4a" and "M4b". For this mode, a horizontal electron displacement in the bending magnet leads to a horizontal shift of the focal point at the streak-camera entrance and correspondingly also on the image of a two-dimensional (2D) streak-camera system, with a horizontal entrance slit instead of a pinhole. With such a 2D system, these shifts and also a transverse size variation may be investigated correlated to the (bunch selective) time distribution. This correlated 2D information leads to considerably deeper insights into beam-dynamics effects, as well as to new quantitative methods [19,27–32]. A comparison of our 2D FSC system with a few other similar devices has been published recently [24].

2.2. General streak-camera characterization

In this section, our streak-camera system (a synchroscan dual-sweep system of type C10910 by HAMAMATSU, Japan) is described in detail. Fig. 2 is used to explain the principle of operation of a synchroscan streak camera in general and to illustrate the specific features of our FSC system. Near the end of the optical beamline, the collimated light beam is focused into the center of the entrance slit (1). The rectangular slit has an effective horizontal width of about 5 mm (defined by the cathode size) for imaging the horizontal beam profile and position in the 2D mode. Using a micrometer scale, the vertical slit height was adjusted to our standard setting of $\Delta y_{slit} = 14\,\mu$m. This height has been optimized for getting enough statistics for single-turn 2D analysis of individual injected bunches [19] and it influences the total time resolution only slightly, as will be quantified below. The light passing the slit enters a mirror-based entrance-optics [33] (2) to focus the spot onto the photocathode without additional chromatic dispersion. The photocathode (3) is a transmission type that emits electrons on the backside (inside the vacuum tube). In order to reduce chromatic dispersion inside the tube, photo-electrons are accelerated by a closely spaced mesh and subsequently focused towards the end of the tube (4).

The fast time information is related to the overall quality of the vertical beam-scanning system coupled electrically to the vertical sweep electrodes (5). A low noise trigger signal obtained from the BESSY 500 MHz master clock via an OPTRONIS 500 MHz to 125 MHz frequency divider [34] provides the fast trigger input, and an internal phase-locked loop reduces the resulting electronic noise. The shortest streak-camera scanning time of 78 ps (so-called time range 1) has been used for all time spectra in this work. Related quantitative resolution values, valid also for our current electronics configuration, have been determined previously [24] for the trigger signals and will be discussed later. The vertical scanning frequency of 125 MHz (ring RF divided by 4) leads to a distance of 8 ns between neighboring bunches on the FSC image. There might be one, two or four rows of different bunches visible on the image, dependent on the time range and on the possible use of our Michelson beam splitter for bunch duplication [24].

Another OPTRONIS frequency-divider chain provides the trigger for the horizontal sweep system, either after each single turn (800 ns)

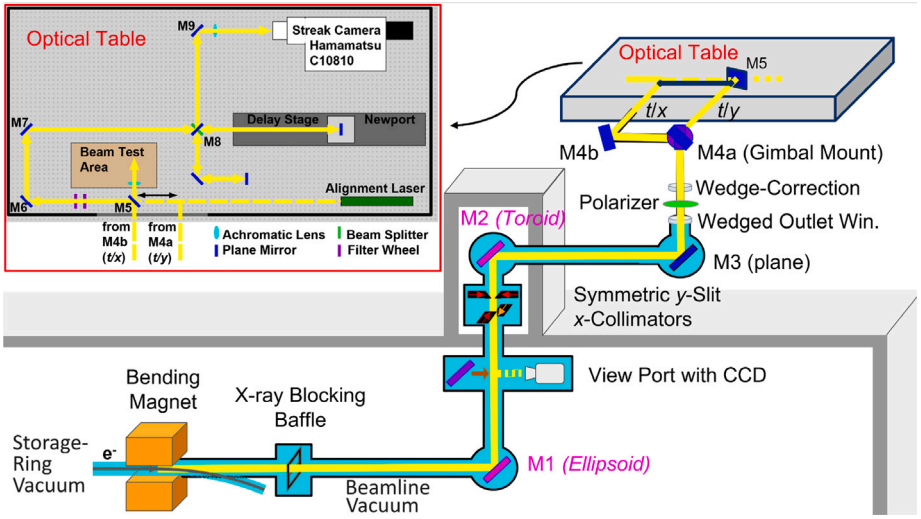

Fig. 1. Sketch of the standard beamline setup installed at BESSY [19]. The storage-ring vacuum is directly connected to the beamline vacuum (marked by light blue color) that ends at the wedged outlet window. In the top-left inset, the optical table is enlarged for better visibility: the "Beam Test Area" block contains also the power meter.

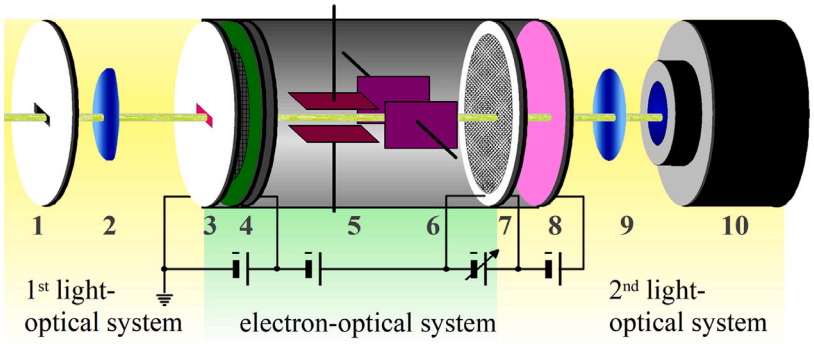

Fig. 2. Sketch of a streak-camera system. The light-optical system is coupled via a photocathode to an electron optical system and via a phosphor screen back to a light-optical system. The main streak-camera elements are an entrance slit (1), the input optics (2), a photocathode (3), an acceleration mesh and a focusing electrode (4), vertical sweep electrodes (5), horizontal sweep electrodes (6), a multichannel plate (MCP, 7), a phosphor screen (8), the output optics (9), and finally a visible-light camera (10).

or after a fixed larger number of turns. This slower (saw-tooth type) scan at the horizontal sweep electrodes (6) allows separating individual bunches within a fixed time window and has been set to a range of 100 ns for all data presented in this paper. The horizontal sweeps are controlled by a modified dual time-base unit M10916-01 (by HAMAMATSU) specifically designed for our 2D system for a maximum blanking amplitude of 1 μs. This unit enables a maximum repetition rate of 1 kHz for rapid pulse accumulation, in comparison to the 10 Hz rate in previous FSC versions. The well known bunch time structure of the storage ring was used for calibrating the slow sweep, and a precision delay stage was used for calibrating the slightly non-linear fast scan axis with sub-pixel resolution via a third-order polynomial [19].

At the end of the streak tube, a combination of multichannel plate (MCP, 7) and phosphor screen (8) yields single-electron sensitivity by generating between about 10^3 and 10^6 photons per converted electron, dependent on the MCP gain. For the high-resolution data presented in this paper, the MCP gain was set to its maximum value. Most generated secondary photons that leave the phosphor screen on the backside enter the 2nd light-optical system, where they are focused by the output optics (9) onto the visible-light detector (10). This detector (10) is an ORCA Flash 4.0 V3 CMOS sensor with 1344 × 1016 used pixels (w × h) and a typical effective frame rate of up to about 60 Hz. Thus, a detector image can be taken for a single-turn illumination [24] or for an accumulation of many turns with a single CMOS frame.

For the time-distribution measurements in this work, we have always used a continuous 1 kHz accumulation for a sum over 5000 frames at 20 ms single-frame exposure time, corresponding to a total time-averaging over about 100 s (100 000 turns).

3. Time resolution studies

In this section, we analyze the different phenomena that may affect the time resolution; these can be classified as wavelength-independent and wavelength-dependent effects. We start analyzing the former and then the latter.

3.1. Wavelength-independent broadening

The uncertainties in the FSC images and the corresponding measured time-spectra are related to external sources outside the FSC as well as internal ones. Here, we present these broadening mechanisms ordered by increasing timing error for the present setup (Table 2)

The smallest contribution comes from a path-length variation of the light transport from the source region inside the bending magnet to the streak camera ($\Delta t_{beamline}$). This was estimated with the ray-tracing program RAY-UI [35] (special version from 2019), by considering the mismatch between electron velocity in the storage ring and vacuum speed of light c as well as the effects of surface roughness and slope errors of the main optical elements.

Another contribution is related to the path-length variation due to the uncertainty of the angular compensation ($\Delta\theta \approx 0.1°$) between

Table 2
List of wavelength-independent time broadening effects, calculated from the square root of the estimated variance.

Parameter	RMS value (fs)
$\Delta t_{beamline}$	≤1.3
Δt_{wedge}	5.5
$\Delta t_{vibration}$	13
Δt_{air}	<20
Δt_{pixels}^{min}	23
Δt_{slit}	89
$\Delta t_{trigger}$	0 ... 295
Δt_{tube}^{asymp}	310

wedged vacuum-exit window and wedge-compensation window (Δt_{wedge}).

$$\Delta t_{wedge} = \sin(\Delta\theta) h_{beam}(n_{fs} - 1)/c. \quad (1)$$

This estimate assumes a collimated beam height of $h_{beam} = 2$ mm (RMS in the wedge direction) and a refractive index of $n_{fs} = 1.46$ for the fused silica window substrates.

Another estimate considers path-length variations due to mechanical vibrations of the light-transport system w.r.t. the storage-ring coordinates ($\Delta t_{vibration}$). Analytically, it is given by

$$\Delta t_{vibration} = \Delta x_{vibration}/c. \quad (2)$$

The use of air-damped legs below the optical table has shifted significant vibration components to frequencies below 12 Hz. Observation of linear interference patterns on the optical table show phase-shift differences of up to about 100 nm every few seconds, pointing to relatively stable positions of optical elements. Measurements with a vibration sensor indicate typical displacements of about 10 µm for the optical table as a whole.

There are various time-delay contributions related to the passage of light through the air (refractive index = 1.00028) after the outlet window. The largest long-time contribution is due to the weather-related local air pressure variation (10 fs drift during some hours). A more critical effect, however, is convective air flow on the optical table on time scales of seconds or minutes. As a countermeasure against such effects, we have used large air-conditioning stages on one wall of the hutch at a temperature of <2 K below the surrounding experimental hall. This leads to mild cooling operation at a low air flux. Further, the coupling between air flow and surface of the optical table is reduced by partial shielding of the main optical path. The only strong power consumer on the surface is the FSC itself, with its heat flow directed away from the optical path. All other devices are either on stand-by or switched off during the experiments. Using a hot-air gun to produce a strong non-equilibrium air flow, we saw significant spatial fluctuations of the light but no timing effect in the FSC image. The value of Δt_{air} in the table is a rescaled upper limit from this test.

Furthermore, there is a geometrical streak-camera resolution component dependent on the slit size and imaging properties of the streak camera.

$$\Delta t_{slit} = M \Delta y_{slit} \Delta t_{pixel}/\Delta y_{pixel}. \quad (3)$$

The height of the entrance slit is $\Delta y_{slit} = 14$ µm (corresponding to the full-width-at-half-maximum or FWHM value of a nearly step-like transmission profile), the total image magnification of the FSC is about $M = 1.84$ as follows from our own measurements, the CMOS pixel size is $\Delta y_{pixel} = 6.5$ µm and one pixel corresponds to $\Delta t_{pixel} = 78$ fs FWHM in the selected (most accurate) time range 1 [19]. As the reference FSC resolution has been determined for $y_{slit} = 10$ µm, our larger slit size introduces an additional time broadening of 63 fs RMS (determined from quadratic summation). This increased slit size is considered in all subsequent numerical evaluations, but leads to a broadening of less than 1% in all cases.

The external 125 MHz trigger signal should introduce no time broadening during an illumination over less than 7 consecutive turns, as follows from the properties of the FSC phase-locked-loop circuit (according to Hamamatsu information). For such short-time measurements, the external trigger drives the FSC circuits and only the noise of these internal circuits will influence the results, as a contribution to the point-spread function. This explains the lowest effective external trigger broadening of 0 fs in Table 2. For extended illumination times, however, there is a net external trigger jitter after filtering that leads to a broadening of the accumulated FSC time distribution dependent on the noise spectrum and short-time drifts after the OPTRONIS RF divider that replaces the corresponding HAMAMATSU module. For the accumulation time of 100 s considered in this work, the trigger jitter extrapolated via a power law is $\Delta t_{trigger} = 295$ fs RMS [24] (see Section 4 for further details). This value includes also the slow temperature drift of about <1 ps between day and night.

At realistic experimental conditions, the internal time broadening of the FSC tube Δt_{tube} yields the largest timing error for analyzing light pulses. It depends to a certain extent on the CMOS pixel size and on the structures of the acceleration mesh and of the MCP. Most important, however, are the influence of the photo-electron spectra on the point-spread function (without streaking scans) and dynamic defocusing effects at the highest scanning speeds [36]. Its minimum value Δt_{tube}^{asymp} at asymptotically large photon wavelengths and for an asymptotically small slit opening is extrapolated as 310 fs RMS. This is an estimated minimum value; however, at realistic experimental conditions, it significantly exceeds this minimum. This effects will be discussed below.

3.2. Wavelength-dependent sensitivity and broadening

In this subsection, wavelength-dependent characteristics of the streak camera system are investigated, in addition to specific transmission properties of the optical beamline (see also Section 3.2.2). This covers spectral intensity determinations as well as delay-time and time-broadening effects. These results will be used for detailed streak-camera timing simulations from the bending magnet to the final camera detection (element no. 10 in Fig. 2).

Fig. 3 displays the quantities concerning production, transport and detection of synchrotron light generated at bending magnet BM2T6R of the storage ring to the streak camera on the optical table. The photon-number spectrum (red curve) has been measured at a position two mirrors behind the wedged-vacuum window, after the mirrors M4a and M4b shown in Fig. 1, using a Thorlabs CCS200 spectrometer for (near) visible light. Thus, these measured data, taken at standard BESSY II beam conditions, involve some light-transfer losses between the source point and the edge of the optical table.

The source spectrum (dashed-dotted magenta curve) stems from a theoretical low-frequency (low ω) standard solution for synchrotron radiation (SR) produced by ultra-relativistic charged particles [37]. The asymptotic frequency-differential power spectrum $\frac{dI}{d\omega} \propto \omega^{1/3}$ is converted to the wavelength-differential photon-number spectrum $\frac{dN}{d\lambda} \propto \lambda^{-4/3}$ that agrees well with the measured spectral shape (photon spectrum) above 500 nm. At lower wavelengths, transmission through the exit window and all mirror coatings before the spectrometer position (probably dominated by the mirrors inside the vacuum system) as well as a minor influence of the X-ray blocking baffle seem to suppress the experimental yield (red curve). The integral over the photon spectrum up to long wavelengths yields a light power of about 7 mW at the end of the vacuum system according to RAY-UI simulations [35] for the standard user mode at 300 mA ring current. Measurements with a power meter were indicating a total light intensity of about 5.5 mW, limited by a reduced infra-red sensitivity of the photodiode sensor and transmission (vacuum window) as well as reflection (two mirrors) losses at short wavelengths.

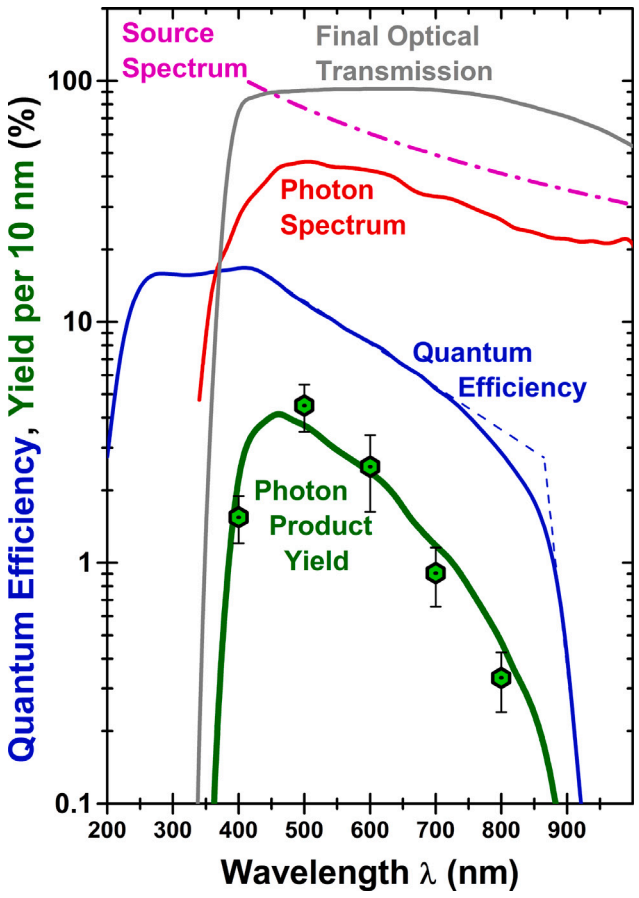

Fig. 3. Wavelength-dependent photon flux and sensitivity of the FSC in a semi-logarithmic plot.

At the entrance edge of the optical table one can optionally guide the light to the FSC or to an analysis stage, which is either the CCS200 optical spectrometer or alternatively the photodiode power meter. The solid gray curve displays the final transmission between this analysis point and the streak-camera entrance, accounting for the various optical modules on this path including the achromatic focusing doublet. This curve shows a maximum transmission value of about 90% at the plateau and strong absorption losses below $\lambda = 400\,\text{nm}$ that are due to anti-reflection coatings on the additional wedge-correction window and on the final focusing lens, as well as protective coatings on the last five mirrors on the optical table. The product of the photon spectrum (red curve) measured at the analysis point and the final transmission function (gray curve) corresponds to the expected wavelength spectrum at the streak-camera entrance.

The displayed cathode quantum efficiencies (solid blue curve) are taken from the FSC test report [38] and exceed even the catalog values. The plateau of the quantum efficiency at $\lambda = [270–440\ \text{nm}]$ corresponds to $16.5 \pm 0.5\%$ emitted electrons at the back-surface per incident photon. The steep asymptotic slope at large wavelengths seems to be consistent with the Fermi edge related to the thermal broadening of the populated electronic density of states at room temperature. Hence, the crossing of the two thin blue dashed lines (at $\lambda = 865\,\text{nm}$) points to a work function of $\Phi = 1.43\,\text{eV}$ at zero temperature for the S-20ER cathode.

The product of the collimated photon rate after the vacuum-exit window, the final light transmission up to the FSC, the quantum efficiency of the streak cathode (the upper three solid curves), and a least-square fitted normalization factor is shown as the green curve named "photon product yield". The height of this curve is proportional to the expected relative streak-camera wavelength sensitivity,

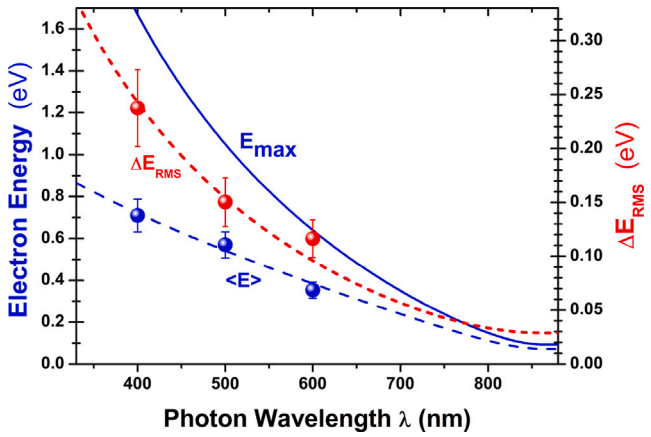

Fig. 4. Wavelength-dependent energy characteristics of photo-electron emission from the photocathode. The solid blue curve is the maximum ejected electron energy E_{max}. The blue markers and the long-dashed blue fit curve show the mean photo-electron energy E_e. The red symbols and short-dashed red fit curve show the RMS peak width $\Delta E_{e,RMS}$ [36].

considering the whole system from the bending magnet to the detector. This green curve is in good agreement with the experimental data (green markers). Five different optical band-pass filters with transmission windows of 10 nm have been used for this comparison. The absolute yield has been derived from the ratio of measured streak-camera intensities with and without band-pass filter (the "white light" intensity corresponds to 100%). The height of the corresponding error bars is dominated by the wavelength uncertainty of the optical band width and the measured focal size at the streak-camera entrance (slightly influenced by wavefront errors). This green curve defines the effective intensity spectrum detected by the FSC. It is used to provide a wavelength dependent weighting of the different dispersion terms within the timing simulations described in Section 4.

3.2.1. *Dispersion effects inside the streak-camera tube*

Fig. 4 displays FSC quantities related to photo-electron emission derived from two different sources. These quantities are the maximum emission energy, the mean kinetic energy and the width of the photo-electron peak. The work function Φ has been extracted from the quantum-efficiency curve measured by Hamamatsu [38] for the S-20ER cathode of our streak-camera tube. The maximum electron energy is approximated by $E_{max} = E_{photon} - \Phi$ for lower wavelengths, and it is added quadratically to a small value (93 meV) that is important for asymptotically large wavelengths. This correction value is related to intrinsic thermal excitations that lead to photo ionization even at the threshold condition (for $E_{photon} = \Phi$) and has been estimated from the corresponding Fermi-Dirac distribution at room temperature and a simple estimate for the surface refraction effect [39].

The blue and red data points are taken from a Hamamatsu investigation [38], extracted from a fit of the curves in Fig. 1 of that paper. These data for an S-20 photocathode are expected to be a reasonable representation also for the S-20ER photocathode inside our streak tube. The original photo-electron spectra are taken with the retarding electric field method, which strongly depends on a hard to quantify transmission function of the retardation optics. Specifically at low energies electron spectroscopy is very sensitive to faint contact potentials inside the scattering chamber and remaining earth-magnetic field effects. Thus, we also expect a limited accuracy for the evaluated spectra and the error bars in Fig. 4 are a rough estimate of the total uncertainties. The dashed curves in Fig. 4 represent least-square fits to the data points, by scaling the solid blue curve and requiring that the resulting fits always stays clearly below E_{max}. These two fit curves are taken as a representation of the energy characteristics of the

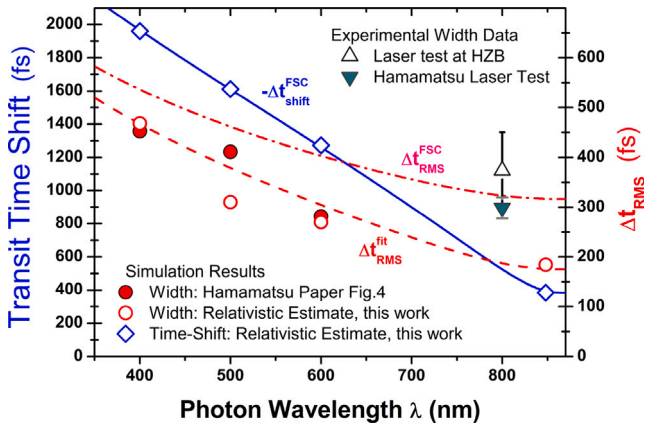

Fig. 5. Wavelength-dependent temporal characteristics of the streak tube. Various computed transit-time spread Δt_{RMS} data are shown in red and relate to the right axis. The closed red symbols are taken from Fig. 4 of Ref. [36]. The measured total time-resolution values determined by Hamamatsu [38] as well as by us [40] for the same streak-camera system under similar conditions are shown as white and olive triangles in the plot and relate to the right axis as well. The blue curve $-\Delta t^{FSC}_{shift}$ shows a computed transit-time shift connected to the left axis. See text for further details.

streak-camera tube, and they will be used as an input for the timing simulations in Section 4.

Fig. 5 displays the main internal timing data of the streak-camera system, namely the time broadening or transit-time spread (red symbols and curves Δt_{RMS}) and a wavelength-dependent mean shift of time distributions (blue symbols and curve, Δt^{FSC}_{shift} with a changed sign). For broadband light detection using filters with a large band width or white light, a variable transit-time shift gives rise to an extra broadening term and will be discussed at the end of this section. Except for the two triangles, all data in this plot have been derived from the calculated so-called transit time, i.e., the time between photo-electron production and electron passage of the fast sweep electrode (No. 5 in Fig. 2). The closed data points for the transit-time spread Δt_{RMS} have been calculated [36] for static electric fields (considering electron acceleration from an S-20 cathode to the deflection electrodes inside a Hamamatsu streak tube) using experimental photo-electron peak widths for λ equal to 400, 500 and 600 nm. The long dashed red curve represents our non-linear least-square fit of $\Delta E_{e,RMS}(\lambda)$ to these three data points, resulting in $\Delta t^{fit}_{RMS} \approx 604\ \mathrm{fs}\ [\Delta E_{e,RMS}(\lambda)/\mathrm{eV}]^{0.46}$.

The dashed-dotted curve named Δt^{FSC}_{RMS} follows from a quadratic summation of Δt^{fit}_{RMS} with 264 fs RMS, a constant term that accounts for all internal wavelength-independent broadening sources for the actual FSC tube and for the reference entrance slit of 10 µm (see Section 3.1). This constant is determined from a fit to the weighted experimental total internal resolution of the streak camera determined with short pulse lasers at 800 nm (the two triangles). Our previous determination of the resolution has resulted in 374 ± 76 fs RMS [40] during the initial FSC commissioning, and the Hamamatsu factory value is 299 ± 21 fs RMS [38]. The dashed-dotted curve Δt^{FSC}_{RMS} will be used in the rest of the paper as an estimate for the total internal streak-camera time resolution related to a fixed photon wavelength (including the small correction for the slit-size extension discussed above).

As stated above, the wavelength-dependent time shift yields another important contribution to the total time resolution for broadband light detection. Variable mean time shifts lead to an additional time broadening via line blending and this may be the dominant resolution term for FSC electron-beam analysis using white light synchrotron radiation. Such time-shift data, however, have not been published by Hamamatsu [36]. Thus, we have performed simplified electron time-of-flight computations using the original photo-electron characteristics and the partly available approximate design data of our streak tube [36,41,42]. We have replaced the on-axis electrostatic field distribution inside the tube by five idealized one-dimensional electrostatic segments with given voltage differences ΔU_i: a constant-field acceleration segment ($\Delta U_1 = 1.85$ kV) between photo-cathode and mesh; a constant-field deceleration segment ($\Delta U_2 = -0.45$ kV) between mesh and focusing electrode, a zero-field drift segment ($\Delta U_3 = 0$) inside the focusing electrode, a constant-field acceleration segment ($\Delta U_4 = 8.6$ kV) between focusing electrode and deflection electrodes, and a short drift segment ($\Delta U_5 = 0$) in between the deflection electrodes, considering relativistic corrections of velocity and acceleration (via the position-dependent relativistic mass increase). Convergence tests point to a numerical accuracy below 1 fs. As an accuracy check, our corresponding results for the absolute transit-time spread are displayed as open red circles in Fig. 5. These values have been calculated using the energy widths shown as red data points in Fig. 4. There is a reasonable agreement of our estimates with the smooth dashed curve and the original Hamamatsu data (closed red circles) in Fig. 5. These original data consider the full potential distributions along the electron flight path, but might also rely on a different (unpublished) energy-peak width determination.

As the transit-time broadening is related to the first derivative of the time-of-flight (TOF) relation, we expect an improved accuracy for the absolute time shift corresponding to the mean photo-electron energy. This mean time shift resulting from our TOF computations is shown by open blue diamond symbols in Fig. 5. The negative sign of $-\Delta t^{FSC}_{shift}$ indicates that the transit-time is reduced in comparison to zero-energy photo-electrons. In other words, a reduced photon wavelength (far below 865 nm) leads to faster photo-electrons inside the tube and hence to a transit-time reduction (a negative time shift). The solid blue curve represents a fit of the blue diamond symbols. This time-shift curve is described by $\Delta t^{FSC}_{shift} \approx -2482\ \mathrm{fs}\ [\langle E_e \rangle/\mathrm{eV}]^{0.709}$ and it will be used in the rest of the paper.

3.2.2. Light dispersion in optical media

Another wavelength-dependent effect in the transport of the photon beam is due to the reduced speed of light in optical media. This leads to peak shifts and a total peak broadening of the streak-camera time projections (Δt^{OTS}_{shift}). The complete photon transport from the source point of the bending magnet to the photocathode will be called optical transfer system (OTS) in the rest of the paper. This includes the vacuum part of the photon beamline, the transfer optics between vacuum window and optical table, and the photon transport on the optical table up to and through the input glass of the FSC tube.

Particularly, this effect is related to the thicknesses and refractive indices of all optical elements as part of the transmission system from the SR source to the streak-camera entrance cathode. The substrate refractive indices of the most important materials used in the optical transfer system are shown in Fig. 6(a). The incident wavelength dependencies for the low-dispersion fused silica (fused quartz) and some standard glasses have been obtained from a web resource [43]. These numerical data are partly extended by product datasheets from Schott, where an overview over dispersion properties can be obtained from an interactive Abbe diagram [44]. Note that the anti-reflection coatings attached to most of the lenses and windows are thin enough (typically $\ll$1 mm) to yield no significant influence on the transmission time. The refractive index n is connected to the incident vacuum wavelength λ_0 dependent phase velocity v_p via $v_p(\lambda_0) = \lambda f = \frac{\lambda_0}{n(\lambda_0) f} = c/n(\lambda_0)$, with the frequency f, $\lambda = \lambda_0/n(\lambda_0)$ and $f\lambda_0 = c$. The important quantity in the current context, however, is the so-called signal transit-time. This reaction delay of a time measurement is given by the signal velocity, which can be defined by the front velocity of a wave packet and might be close to the vacuum speed of light c in the case of a high-detection sensitivity and wave-packet broadening as a result of dispersion [37,45].

For the current experimental setup, however, the signal velocity is equal to the group velocity v_g and describes the mean motion (the center motion) of the envelope of the light pulse. The group velocity

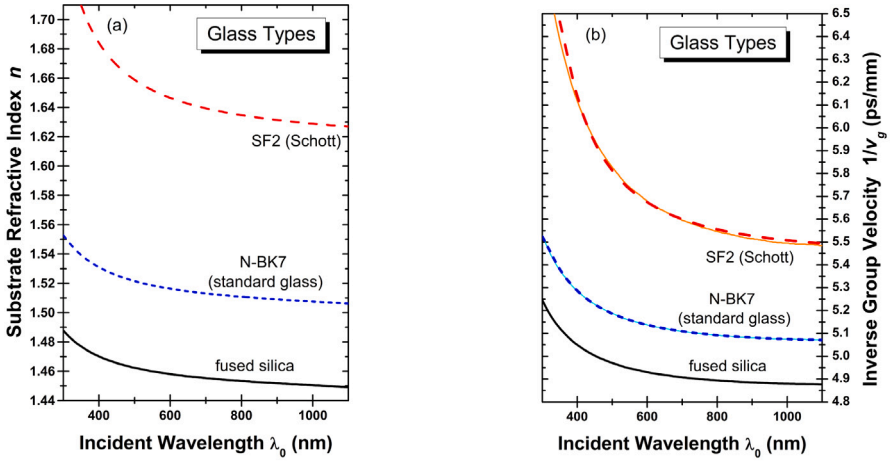

(a) Refractive index. (b) Inverse group velocity.

Fig. 6. Refractive index n and inverse group velocity as function of the incident (vacuum) wavelength λ_0. Shown are those optical glass types (fused silica, N-BK7 and SF2) that are part of our transfer system between the in-vacuum mirrors and the streak-camera entrance.

is defined by $v_g(\lambda) = \frac{\partial\omega}{\partial k} = \frac{\partial(2\pi f)}{\partial(2\pi/\lambda)} = \frac{1}{\frac{\partial(1/\lambda)}{\partial f}}$ with the wave number k, leading to $v_g(\lambda) = \frac{c}{n} + f\frac{\partial n}{\partial f}$ after replacement of variables and application of the product rule. For the standard case of normal dispersion, $\partial n/\partial f$ is positive and is enhancing the dispersion term for the group velocity. This corresponds to $\partial n/\partial\lambda_0 < 0$ as can be seen in Fig. 6(a) for all considered glasses.

Fig. 6(b) displays the inverse group velocity, which is proportional to the time delay of light within optical materials. The resulting total transmission delay of an optical compound system is given by $\Delta t^{OTS}_{shift} = \sum_j l_j/v_{g,j}$, where l_j and $v_{g,j}(\lambda)$ are the thickness and the group velocity of a specific material j, with substrate refractive index $n_j(\lambda)$. For some materials, however, the published refractive index values do not reach far enough into the short wavelength regime. Thus, we decided to use experimental data for fused silica (with reliable values in the range 200–2000 nm) as a reference for the description of other materials. The inverse group velocity of each material j is then represented by the linear scaling

$$\frac{1}{v_{g,j}} = P_{1,j}\left(\frac{\partial k}{\partial\omega}\right)_{Silica} + P_{2,j}, \tag{4}$$

and the corresponding fits of the two parameters P_1 and P_2 for each material have been performed for wavelengths λ_0 in the range 380–780 nm that dominate the photon product-yield in Fig. 3. The results of this dispersion scaling are shown in Fig. 6(b) for SF2 and N-BK7 glass as solid thin curves. The difference between the thin solid fit curves and the thick dashed curves derived directly from experimental data involves a standard deviation of only 0.2% for SF2 and even less for N-BK7. Thus, the fits are in very good agreement with existing data (see Fig. 6(b)) and extrapolation outside the published wavelength regions of other materials is expected to be accurate as well. In total, we have performed such fits for the 4 different materials that are contained in our OTS in addition to fused silica and the fit parameters are shown in Table 3. The parameter P_1 is directly related to the wavelength dispersion of the photon TOF within a material normalized to fused silica. It means, that, for instance, the TOF dispersion within SF2 glass exceeds the one of fused silica by a factor of 3.673 at equal thickness at the same wavelength. In the following numerical timing simulation we have used the scaling with P_1 and P_2 for obtaining accurate results for the dispersion as well as for the mean time delay for the given combination of optical materials in the transmission system.

Table 3
Linear scaling parameters P1 and P2, for the interpolation of incomplete data sets, fitted to the wavelength range 380–780 nm using fused silica as a reference material for the inverse group velocity (Eq. (4)).

Material	P_1	P_2 (ps/mm)
N-BK7 (std glass)	1.245	−0.803
SF2 (Schott)	3.673	−3.384
Soda Lime	1.200	−0.630
SF5 (Schott)	4.086	−3.516

4. Timing simulations

Fig. 7 shows the various time-dispersion terms discussed above for the full calculated spectrum (white-light) given by the photon product yield in Fig. 3. The corresponding Monte-Carlo solution is explained in Appendix. For simplicity, the temporal resolution is displayed as a function of the glass thickness d_{fs} of a hypothetical optical system consisting of fused silica modules only. For a data-acquisition time $t_{acq} \ll 5\,\mu s$ (single-shot data acquisition), as assumed here, the internal FSC phase-locking hardware should suppress all external trigger-jitter components.

The dashed pink curve named "deterministic dispersion simulation" displays the standard deviation (right axis) of the resolution due to the sum of two time-shift terms averaged over the effective white-light spectrum. This involves Δt^{FSC}_{shift} related to the mean photo-electron energy inside the streak tube and Δt^{OTS}_{shift} due to the modified speed of light in the optical media. At the glass thickness $d_{fs} = 0$, the deterministic width is solely given by the wavelength-dependent time shift inside the FSC tube. In principle, the time delay within optical media is proportional to the glass thickness d_{fs}; however, as discussed in Section 3, the time shifts Δt^{FSC}_{shift} and Δt^{OTS}_{shift} involve opposite signs. The corresponding delay-time cancellations lead to a minimum of the dashed curve around $d_{fs} = 8\,mm$. The non-zero resolution at the minimum reflects the different wavelength dependencies and, thus, an incomplete cancellation of both time-shift terms.

The solid pink curve named "full dispersion simulation" considers all simulation terms for single-shot operation (no trigger jitter), and it shows the standard deviation resulting from the square root of the numerically determined variance. In addition to the deterministic dispersion, the stochastic term due to the wavelength-dependent transit-time jitter Δt^{FSC}_{RMS} (dashed-dotted curve in Fig. 5) is fully considered. This involves the wavelength-dependent variation of the photo-electron

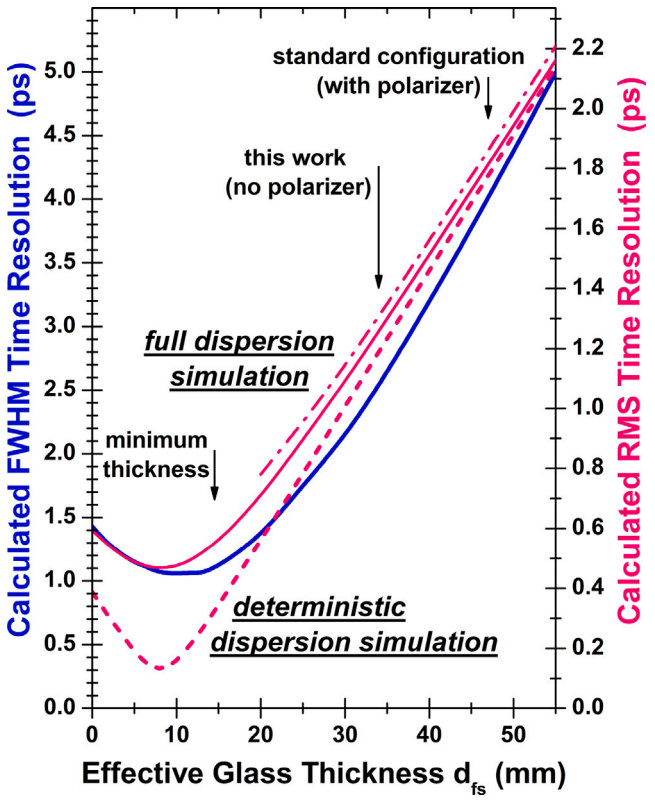

Fig. 7. Calculated bunch-length resolution for white-light SR (wavelength range 325–1000 nm) referenced to a pure fused silica thickness as a replacement of the involved optical materials. The dashed curve stands for a deterministic simulation by accounting the wavelength dependent time delays only. All other curves, named "full simulation", involve additionally the wavelength dependent stochastic broadening (see text for further details).

spectra in the FSC tube and also all wavelength-independent contributions discussed in Section 3.1. Analyzing the white-light broadening fractions of the solid pink curve yields a main contribution by Δt_{RMS}^{FSC} for $d_{fs} < 16$ mm, where the dispersion terms related to time shifts inside the tube and inside the OTS are reduced by their mutual cancellation. Above $d_{fs} = 18$ mm, Δt_{shift}^{OTS} yields the dominant contribution to the time resolution for single-shot data acquisition. The dashed-dotted curve includes the additional broadening related to a long data-acquisition time of $t_{acq} = 100$ s, which might be interesting for bunch charges in the sub-pC regime. Comparison with the solid pink curve yields an influence due to the trigger jitter $\Delta t_{RMS}^{trigger}$ of only about 4% on the final resolution for white-light SR.

Quantitative comparison of the x-axis in Fig. 7 with our streak-camera transmission system is performed by considering the scaling parameters P_1 (see Table 3) that describe the wavelength dispersion for each device relative to fused silica. The arrow denoted "minimum thickness" points to the effective fused silica thickness of 14.5 mm, given by a 4 mm vacuum exit window and the FSC entrance glass window in front of the FSC cathode (as we did not receive sufficient information on the thickness and specifically on the dispersion of this glass, this is probably the most uncertain part of the OTS parameters). Thus, the left most arrow indicates the minimum glass configuration where the final focusing would be performed with a focusing mirror. Such a configuration has been tested experimentally during the initial setup of our FSC system, but turned out to be inflexible and optimization was extremely time-consuming. Hence, we decided to use an achromatic doublet lens for simple and flexible focusing of the light onto the FSC entrance window. Furthermore, the vacuum exit system involves two wedged windows rotated by 180° around their axis (for suppression of reflections and spatial dispersion). The middle arrow in the plot marks this effective glass thickness of 34 mm used in this work. It corresponds to an RMS time resolution of about 1.3 ps for single-turn single-bunch acquisition using white light. For other measurements the use of a polarizer improves the spatial resolution in the transverse direction, and it corresponds to another 13 mm effective glass thickness as indicated by the right-hand side arrow. This single-shot configuration for injection and kicker dynamics corresponds to a RMS time resolution of 1.8 ps (about 1.4 ps for our previous setup [19] without anti-wedge correction window).

The solid blue curve displays another numerical evaluation of the "full dispersion simulation", namely the FWHM resolution (left axis) for each effective glass thickness. This FWHM evaluation is based on an automated shape analysis of the simulated time distribution after time binning. The FWHM axis on the left-hand side is proportional to the standard deviation axis on the right, with a scaling factor of 2.355 (Gaussian distribution). Both evaluations are roughly consistent for glass thicknesses below 5 mm and around 60 mm. At our current working conditions (middle arrow in Fig. 7), however, there are deviations between by about 20%. Specifically, the steep decay of the inverse group velocity at low wavelengths leads to an asymmetric time distribution. This indicates that the light spectrum in the FSC should be restricted to wavelengths above 500 nm for improving the time resolution. Tests show that convolutions of the asymmetric time distributions with Gaussian functions are in good agreement with quadratic summation of the corresponding RMS values, in contrast to the FWHM values. Further, relative numerical errors of our FWHM evaluation exceed the ones of RMS results by up to one order of magnitude. Thus, all subsequent bunch-length evaluations are presented as RMS values.

In addition to the increased timing-slit width discussed above, also a finite trigger jitter needs to be accounted for the simulations in the next section. This is done by adding both extra broadening terms quadratically to the Gaussian Δt_{RMS}^{FSC} term of the simulation. Beyond the single-trigger condition, there is an uncompensated finite trigger jitter that depends on the data-acquisition time t_{acq}. Following the previous analysis of noise and short-time drifts of our OPTRONIS RF divider (500 to 125 MHz) in combination with the Hamamatsu C10910 FSC [24], the approximate RMS trigger jitter is given by Eq. (5)

$$\Delta t_{RMS}^{trigger} = 0.145 \text{ ps } [t_{acq}/\text{s}]^{0.154} \tag{5}$$

and used in all subsequent simulations.

5. Experimental results at BESSY-II

Measurements and simulations have been performed with additional filters made of fused silica (Thorlabs FELH edge filters of 2 mm thickness and Edmund band-pass filters of 3.5 mm thickness). For very narrow band-pass windows, the deterministic time shifts do not contribute to the resolution and the values are dominated by the curve for Δt_{RMS}^{FSC} in Fig. 5, independent of the effective glass thickness. This interplay of filter type, filter bandwidth, filter wavelength and time resolution at acceptable photon-counting statistics will also be investigated to find the optimal configuration.

If not indicated otherwise, we compare different FSC measurements with the corresponding full simulations for a constant data-acquisition time t_{acq} of 100 s in order to reach a counting statistics that is sufficient also for small bandwidth filters at large wavelengths. This data-acquisition time corresponds to a summation of 10^5 illuminations at the synchroscan repetition rate of 1 kHz with an extrapolated uncompensated jitter of $\Delta t_{RMS}^{trigger} = 295$ fs (see Eq. (5)). Based on our previously determined absolute photon counts [24], a yield of only about 1 detected photon per bunch per turn is estimated for the data in the next figure for a line filter at 700 nm with 50 nm bandwidth and even less for a filter with only 10 nm bandwidth. This low probability explains the need for such a large number of illuminations. For the subsequent simulation results, the linear scaling parameters P_1 and P_2

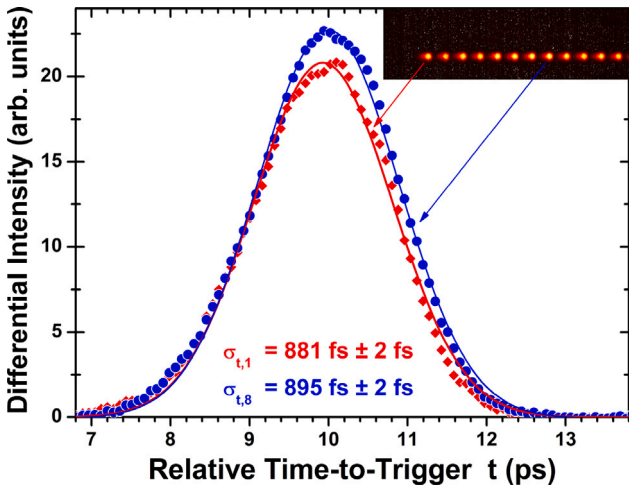

Fig. 8. Measured FSC time spectra for two bunches (with fitted Gaussian curves) of a continuous bunch train after an extended gap in the fill-pattern distribution. The inset displays a color-coded plot of the streak-camera image for an investigated 100 ns fraction of the fill pattern, with a distance of 8 ns between the observed bunches (horizontal direction of the inset). The vertical direction in the inset corresponds to the fast timing axes.

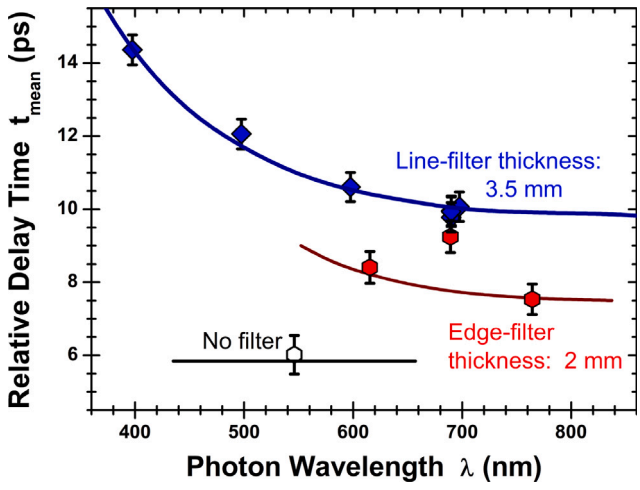

Fig. 9. Mean temporal peak position for white-light SR as well as for limited wavelength regions after passing either through a band-pass filter or through an edge filter. The measured results are indicated by the markers, and are placed horizontally at the mean λ determined from each filter spectrum (given by Fig. 3 and specific limits). The corresponding simulations are displayed by continuous curves with the same λ mean definition as used for the experimental data points.

of Table 3 are considered for each element of the optical transmission system. Thus, delay time and time resolution are computed on equal footing.

The BESSY II storage ring was optimized for generating extraordinary short bunches at stable ring conditions. The ring was thus tuned empirically towards a momentum compaction factor $\alpha \rightarrow 0$, where the zero-current bunch-length should reach a minimum that depends on various machine properties. This tuning leads to a very low synchrotron frequency of roughly 400 Hz. 336 out of 400 buckets have been filled with bunches of similar intensity. Scraping procedures have been applied in order to reach sub-μA bunch currents, where all types of collective effects are strongly suppressed. Finally, the bunch currents were as low as $I_{bunch} = 850 \pm 120$ nA, where the large uncertainty of the mean bunch current includes the noise of the average current determination and the bunch-to-bunch variation of the light intensity measured with the streak camera. Note that the current and the bunch pattern were very stable during the complete data acquisition over about 1 h.

The FSC time spectra in Fig. 8 have been obtained for synchrotron light filtered by an optical band-pass at a central wavelength of 700 nm and bandwidth of 50 nm. This relatively large bandwidth leads to large count rates and, thus, to small statistical uncertainties that are favorable for the comparison of different bunches within a bunch train. For all spectra, we have projected each pixel value onto the fast time axis (vertical direction in the inset), by summation inside an equidistant (slow scan) region of interest around each bunch maximum. A background defined by the last empty bucket in the gap (left of the red arrow) has been subtracted, and the pixel-based data have been converted into time units by considering also the intensity transformation from yield-per-pixel to yield-per-ps. The relative pulse lengths extracted from Gaussian fits differ by less than ±1.5%, and the mean RMS value for the bunches shown in the inset of Fig. 8 is 0.894 ps. As one can see, the two spectra in Fig. 8 are slightly asymmetric, and the mean positions are also shifted in time. This position variation is below ±40 fs or ±0.5 CCD pixels of the FSC for all measured bunches. Both, position and pulse-length variations are very small and might be related to minor non-linearities inside the FSC hardware (partly also due to the asymmetric photo-electron energy spectra).

In the following, we will compare experimental data for line filters as well as high-pass wavelength filters at multiple characteristic wavelengths with the corresponding simulation results. Dependent on the type of filter and on the measured quantity, different simulation terms can be tested. For improving the experimental precision of our analysis, we have always evaluated the same set of bunches for the determination of mean temporal width and position data as well as for estimating the corresponding uncertainties of the experimental data.

In Fig. 9, the mean peak positions in time, respectively the mean delay times, are investigated as a function of photon wavelengths for different types of filters and white light. These data do only depend on the deterministic time shifts due to the dispersion inside the FSC tube and inside the OTS. The different experimental position data in the figure are directly obtained from the projected time spectra at fixed settings of internal FSC time range and delay. This means that the experimental values are relative to the master clock of the storage ring, plus a constant delay time. For comparing simulation and experiment, we have corrected all simulated delay times by a common fixed offset value (associated to cable lengths as well as constant electronic delays inside and outside the FSC) determined from a least-square fit to the experimental line-filter results.

Four of the band-pass filters have a bandwidth of 10 nm centered at wavelengths of 400, 500, 600 and 700 nm. There are two solid diamond markers at a wavelength of 700 nm but with different bandwidths and slightly different weighted photon wavelength. The point at the nominal wavelength corresponds to the bandwidth of 10 nm. The point displaced slightly to the left for better visibility corresponds to a bandwidth of 50 nm. These two values agree to within the error bars and thus, we do not notice any significant dependence on the bandwidth. The blue simulation curve agrees very well with the experimental data and its steep rise towards small wavelengths is given mainly by the inverse group velocity of Fig. 6(b) (slightly reduced by the negative time shift inside the FSC tube as displayed in Fig. 5).

The white-light measurement (no filter) is shown by the open hexagon with the underlying simulation result represented by the solid black line, and the horizontal size of this line indicates the FWHM of the photon product yield (220 nm as determined from Fig. 3) that contributes to the measured mean delay time. Again, we find a good agreement between experiment and simulation by using exactly the same offset used for the band-pass filter data.

The other three red hexagon symbols belong to Thorlabs premium hard-coated long pass filters, with lower cut-off wavelengths of 500, 600 and 700 nm (the corresponding widths of the filtered photon spectra are

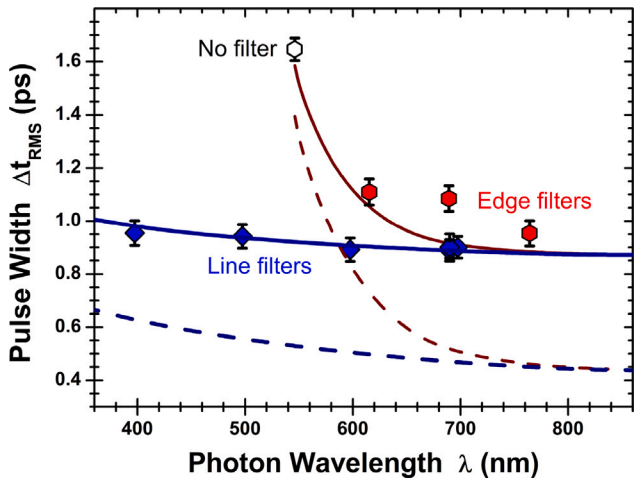

Fig. 10. Mean temporal peak width for white-light SR, as well as for specific wavelength regions, after passing either through a band-pass filter or through an edge filter. The measured data points and the simulated curves are placed horizontally at the mean λ of the corresponding spectra (see Fig. 3).

somewhat below the white-light case and reduce with increasing cut-off wavelength). The delay times for the filter edges at 500 and 700 nm agree well with the corresponding simulations. The 600 nm edge filter, however, shows a significant deviation from the simulation. An optical inspection of this filter did not show any obvious problem.

The difference of 2.20 ± 0.15 ps between the band-pass filter simulation and the edge-filter simulation is mainly given by the substrate thickness difference of 1.5 mm multiplied by the inverse group velocity in fused silica reduced by the inverse vacuum speed of light. To within an uncertainty of 10%, the same scaling enables also to transform the no-filter result at 546 nm (average wavelength) to the blue curve at the same wavelength. The remaining deviations are expected to be due to the asymmetric wavelength dependencies around the hexagon data points, covering large wavelength ranges.

The aim of Fig. 10 is the comparison of the measured pulse duration with the simulated resolution function and the (unknown) electron bunch length. The blue dashed curve shows the simulated time resolution for 10 nm band-pass filters, while the brown dashed curve displays the resolution corresponding to the use of edge filters at various cut-off wavelengths. The measured peak widths are displayed by symbols and can be understood as a convolution of the constant temporal distribution of the electron bunches in the storage ring (consisting of the intrinsic bunch shape and a minor influence of ring fluctuations and drifts during the data-acquisition time) and the total time resolution of the FSC system. Thus, the solid blue curve is determined through a least-square fit of a broadened resolution function to the measured line-filter pulse widths, resulting in an RMS electron bunch length of $\Delta t_{RMS}^{bunch} = 0.75 \pm 0.01$ ps (added quadratically to the stochastic Gaussian width Δt_{RMS}^{FSC} in the simulation). This value for Δt_{RMS}^{bunch} is very close to a previously determined bunch length for similar beam parameters of BESSY II via spectroscopy of coherent THz radiation [15]. The solid blue curve agrees perfectly well with the experimental band-pass filter data (closed blue diamonds). For these narrow bandwidth filters, the measured peak-width variation is dominated by the stochastic time broadening of the streak-tube electrons Δt_{RMS}^{FSC} resulting from the photo-electron energy distribution emitted by the FSC cathode. The two solid diamond markers with different bandwidths at a common wavelength of 700 nm agree well, as in Fig. 9. Hence, the data point for the larger bandwidth of 50 nm, slightly displaced to the left, is not significantly influenced by an additional delay-time broadening.

The solid brown curve is derived from the dashed brown curve using the same bunch-length value. For the wide range of wavelengths

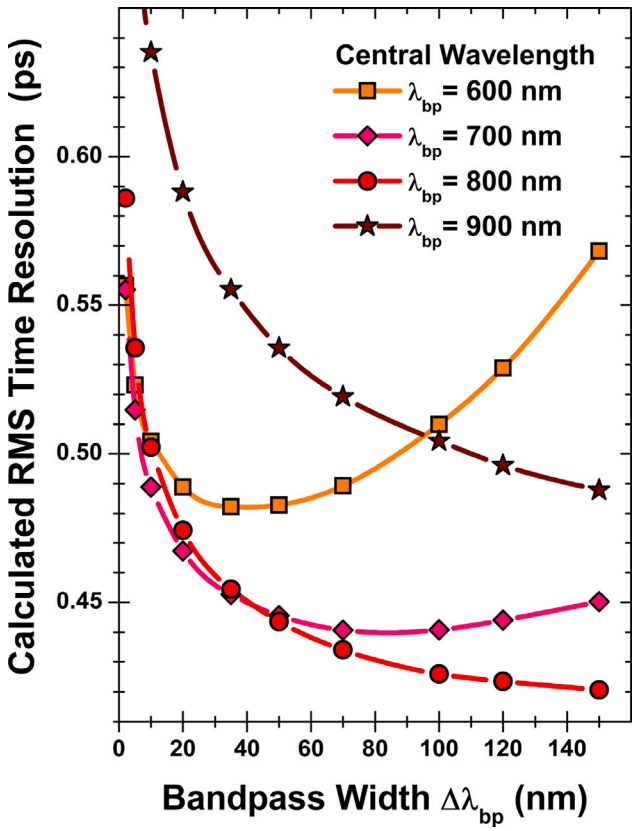

Fig. 11. Mean temporal resolution (RMS) for filtered SR, calculated as a function of the band width $\Delta\lambda_{bp}$ for different band-pass filters at central wavelengths λ_{bp} from 600 to 900 nm.

covered by the white-light case and by the edge filters, however, both time-shift terms (Δt_{shift}^{FSC} and Δt_{shift}^{OTS}) in addition to the photo-electron time-broadening term Δt_{RMS}^{FSC} come into play. If we exclude the result for the 600 nm edge filter, the wide-range simulations (solid brown curve) lie about 6% below the edge-filter data points at 500 and 700 nm. The deviation between the white-light data point (taken without any wavelength filter) reaches 9%, when compared to a simulation for the same OTS configuration. Based on the good agreement between experimental and simulated band-pass filter results in Figs. 9 and 10, the three dispersion terms can be ruled out as major causes of this deviation. Thus, it might be related to neglected higher-order effects in the simulation, such as a non-Gaussian FSC photo-electron time broadening. Other possible uncertainties might be hidden in the accuracy of the photon product-yield (see Fig. 3) that determines the wavelength-averaging process or of the assumed FSC tube parameters for the delay compensation of both time-shift terms at large wavelengths, where there are no band-pass filter data. In addition, we find an extraordinarily large deviation of the experimental 600 nm edge filter results from the simulated curves in Fig. 10 as well as in Fig. 9. One might speculate that such an effect might be related to a resonance-like delay and broadening effect induced by multiple light reflections at some frequencies in the specific layer structure of the interference filter coating itself.

The reasonable overall agreement between experiment and simulation in Figs. 9 and 10 indicates a detailed quantitative understanding of the different temporal delay and broadening mechanisms. Given the conceptual design of the SR source and the optical transfer system, there are only few parameters that allow to tune the time resolution for diagnostics of a stable stored electron beam. A corresponding optimization of the FSC timing is presented in Fig. 11. It displays simulations for four different central wavelengths. We kept the FSC entrance timing

slit at a constant opening of $y_{slit} = 14\,\mu m$, but varied the central filter wavelength λ_{bp} and filter bandwidth $\Delta\lambda_{bp}$, as well as the data-acquisition time in the simulation. As can be seen from the dashed lines in Fig. 10, larger wavelengths and smaller bandwidths lead to an improved time resolution. However, this leads to a loss of intensity and requires an increased data-acquisition time, resulting in an increased effective trigger jitter $\Delta t_{RMS}^{trigger}$ (see Eq. (5)).

This tradeoff between reduced wavelength dispersion and reduced trigger noise requires choosing a data-acquisition time that keeps the statistical uncertainty (or the filtered photon fluence) constant. For the results in Fig. 11, the data point at $\lambda_{bp} = 600\,nm$, $\Delta\lambda_{bp} = 10\,nm$ and a data-acquisition time of $100\,s$ serves as a reference point. This is also the same value for the $600\,nm$ case of the dashed blue curve in Fig. 10. For all other results in Fig. 11, the acquisition time is scaled proportional to the inverse bandwidth and to the inverse photon product yield in Fig. 3 to yield a constant FSC intensity. The corresponding broadening $\Delta t_{RMS}^{trigger}$ by electronic trigger jitter is adjusted for each evaluated data point separately.

On the left side of the plot, one may see a rise of each curve due to the increased trigger jitter at large data-acquisition times. The flattening or rise for large bandwidths is mainly related to the temporal wavelength dispersion inside the optical transfer system. From the plot, one may conclude that a band-pass filter at a wavelength around $800\,nm$ with a large bandwidth somewhat above $100\,nm$ leads to an optimum RMS time resolution below $0.43\,ps$; however, a high quality filter with this property seems not to exist.

Finally, the $900\,nm$ curve, shows a large worsening of the time resolution: this is due to the very low photon product yield at that wavelength (see Fig. 3) and the corresponding long data-acquisition time and the resulting large trigger jitter.

6. Conclusion

In this work, we have investigated in great detail the temporal properties of our streak-camera system at the BESSY II light source in Berlin. This system involves large opening angles matched to the custom-made focusing mirrors that lead to a low spatial diffraction limit and also to a high photon flux, enabling even high-resolution 2D single-shot measurements at a bending magnet [19,24]. A large part of this paper deals with the physics of light transport to the FSC as well as with photo ionization and electron dynamics inside the FSC. For the first time, the various time-resolution terms for finite wavelength regions in addition to the electronic noise broadening have been considered consistently for a complete FSC system from the photon-source point to the final detector.

The electron storage ring was tuned empirically towards the shortest bunches by reducing the momentum compaction factor as well as by restricting the bunch charges. Bottom-up simulations for various band-pass and edge-wavelength filters prove that we have experimentally reached an overall time resolution of $0.47\,ps$ RMS using filtered synchrotron light for pC bunch charges. Comparison of experimental and simulated peak widths yields an all-over bunch length of $0.75\,ps$ RMS averaged over a data acquisition time of $100\,s$ for the BESSY II storage-ring conditions used in this investigation.

For single-shot experiments (single-turn and single-bunch) at bunch charges above about $0.2\,nC$, one needs as much light as possible and white-light FSC operation without wavelength filtering is advised. This method has been used for measurements of either an injected or a kicked bunch at BESSY II [19]. For this case, our 2D streak-camera system reaches a time resolution of $1.3\,ps$ RMS (about $1.8\,ps$ for an optimized spatial resolution). If optimum time resolution is the main goal and if there is no need for flexibility (important for different 2D modes or modified spatial magnification), one may reach a single-shot time resolution of about $0.55\,ps$ RMS as determined by the simulations for white-light illumination. In such a system, the achromatic lens has to be replaced by a mirror-based focusing at the end of the transmission optics and both wedged windows have to be replaced by a single vacuum-exit window (leading to reflections and thus a reduced dynamic range of the FSC).

For low bunch currents in the μA regime, single-shot measurements with high resolution are hardly possible with SR from a bending magnet. Under this condition, an extended multi-turn data accumulation is important, but it introduces a loss of time resolution due to an uncompensated trigger jitter. Fortunately, this jitter rises only slowly with the data-accumulation time and additional wavelength filtering may significantly improve the total FSC time resolution. As shown in this work, we have reached a time resolution of $0.47\,ps$ RMS for two types of band-pass filters at the central wavelength of $700\,nm$ for very low bunch currents (using an OPTRONIS low-noise divider for conversion of the master clock signal). An even better total resolution of about $0.43\,ps$ RMS could be achieved with a $800\,nm$ band-pass filter at a bandwidth above $100\,nm$. A search for such a device at a few well-known optical filter producers, however, was not successful. Of course, there are optical filters at the central wavelength of $800\,nm$, but not with large bandwidths, low-transmitted wavefront errors (important for high transmission and spatial 2D resolution) and large optical densities for the suppression of smaller wavelengths.

Finally, comparison with experimental data for white light and different types of filters indicates a good understanding of the time-resolution effects related to synchroscan streak-camera measurements. The simulation methods are applied to bending-magnet based SR in this work. However, the used methods are very general and other broadband or multi-band light sources (synchrotron radiation from insertion devices, laser based higher-harmonic generation or plasma-generated light emission) in combination with a streak camera could be treated quantitatively in a similar way.

Furthermore, the high accuracy that we have reached for the time resolution of the streak-camera system enables future advanced beam-dynamics measurements. Specifically, this covers extreme short-pulse storage-ring conditions, where the low-current onset of collective effects could be investigated in detail.

CRediT authorship contribution statement

G. Schiwietz: Writing – review & editing, Writing – original draft, Visualization, Validation, Supervision, Software, Project administration, Methodology, Investigation, Formal analysis, Conceptualization. **M. Koopmans:** Writing – review & editing, Validation, Methodology, Investigation. **Ch. Kalus:** Writing – review & editing, Methodology, Investigation. **M. Marongiu:** Writing – review & editing, Validation, Investigation. **A. Schälicke:** Writing – review & editing, Validation, Investigation. **P. Schnizer:** Writing – review & editing, Investigation. **M. Ries:** Writing – review & editing, Methodology, Investigation, Conceptualization.

Declaration of competing interest

The authors declare that they have no known competing financial interests or personal relationships that could have appeared to influence the work reported in this paper.

Data availability

Data will be made available on request.

Acknowledgments

This work is supported by the German Bundesministerium für Bildung und Forschung, Land Berlin and grants of the Helmholtz Association. We acknowledge hardware developments for the timing beamline by Th. Zeschke, R. Fleischhauer, O. Pawlizki and I. Müller. Further, we acknowledge the software support by Th. Birke and I. Seiler, the incorporation of realistic time structures into the ray-tracing code RAY-UI by P. Baumgärtel, and very helpful discussions and information by I. Grill and Th. Franzl from the Hamamatsu support group.

Appendix. Numerical procedures

The numerical solutions described in this appendix include all the discussed time-broadening and delay effects in a Monte Carlo simulation. The sub steps and program functions have been checked separately to agree with the input data from Section 3. A python program simulates the stochastics of 10^6 individual photon-electrons produced inside the FSC tube for each case under consideration. The corresponding photons are generated within a maximum wavelength range from 325 to 1000 nm for "white-light" and their differential probability follows the photon product yield in Fig. 3. Compared to the white-light case, the wavelength range for band-pass filters or edge filters is restricted via a hit or miss algorithm assuming step-like transmission profiles.

In detail, the following steps relate to each of the Monte Carlo events: a wavelength λ_i for a test photon is randomly selected according to the all-over detection probability of the FSC system. However, prior to the first wavelength selection, the photon product yield (see Fig. 3) is integrated from 325 nm to any upper limit of λ_{ini} yielding the normalized cumulative distribution function $0 \le \phi(\lambda_{ini}) \le 1$. The actual wavelength is then computed from a random number between 0 and 1 that is used to determine λ_{ini} via numerical inversion (tabular search and linear interpolation of the stored cumulative distribution function). Hence, the stochastic sequence λ_i represents the synchrotron light spectrum modified by the optical transmission function and the quantum efficiency of the cathode (S-20ER) of our streak camera. The direct conversion of each random number to λ_{ini} may often lead to non-acceptable values outside the limited wavelength regions determined by band-pass filters or edge filters (not included in the cumulative distribution function). For these cases, an offset value and a squeezing factor is applied to transform the random number range to the expected values for the specific wavelength region. Specifically for band-pass filters with a small bandwidth, this reduces the computation time by an order of magnitude without re-calculating the cumulative distribution function. As a numerical check of the procedures, wavelength binning is applied to the sequence λ_i. The resulting stochastic wavelength spectrum without filter agrees with the photon product yield displayed in Fig. 3 to within the statistical uncertainties.

Next, the deterministic total time shift is computed for the wavelength λ_i. This involves the negative time shift of the streak-tube electrons Δt^{FSC}_{shift} at non-zero photo-electron energies (see Fig. 5). Furthermore, the positive time shift inside the optical transfer system Δt^{OTS}_{shift} is also accounted for.

Another stochastic term that has to be considered is the transit-time distribution of electrons from the FSC cathode to the deflector electrodes. For a fixed wavelength, the corresponding time broadening is given by Δt^{FSC}_{RMS}, resulting from the corresponding photo-electron energy peak-width that reflects the electronic density of states at the surface, surface electron refraction and the dipole transition-matrix elements for excitation into low-energy continuum states. Here we approximate the time variation within the photo-electron peak by a Gaussian characterized by Δt^{FSC}_{RMS} and, thus, we use an error-function routine as a normalized cumulative distribution function.

Each final event-detection time is used in a cumulative way to determine the mean delay time, the time variance as well as the differential time spectrum (via binning). This enables a full characterization of the beam diagnostical system, independent of the beam or machine properties.

References

[1] G. Kube, Review of synchrotron radiation based diagnostics for transverse profile measurements, in: Proc. of DIPAC, Vol. 35, 2007, pp. 6–10.

[2] T. Lefevre, Bunch length measurements, in: Proc. of CERN Accelerator School, Intermediate Level, 2015.

[3] J. McKenzie, S. Buckley, L. Cowie, P. Goudket, M. Jenkins, B. Militsyn, A. Moss, A. Wheelhouse, G. Burt, A. Wolski, Bunch length measurements using a transverse deflecting cavity on VELA, in: Proceedings of the 7th International Particle Accelerator Conference IPAC'16, JACoW, 2016, pp. 323–326.

[4] Q. Zhao, J. Bahr, I. Bohnet, K. Flottmann, D. Lipka, D. Richter, F. Stephan, Design of the bunch length measurement for the photo injector test facility at DESY zeuthen, in: Proceedings of the 2001 Particle Accelerator Conference (PAC2001, Cat. No. 01CH37268), Vol. 3, IEEE, 2001, pp. 2299–2301.

[5] F. Hartemann, W. Brown, D. Gibson, S. Anderson, A. Tremaine, P. Springer, A. Wootton, E. Hartouni, C. Barty, High-energy scaling of compton scattering light sources, Phys. Rev. Spec. Top.-Accel. Beams 8 (10) (2005) 100702.

[6] K. Holldack, T. Quast, S. Khan, R. Mitzner, Bunch shape diagnostics using femtoslicing, in: Proc. of the European Particle Accelerator Conference EPAC2006, 2006, p. 3305.

[7] D. Malyutin, A. Matveenko, et al., Electron beam probe diagnostic for BESSY II storage ring, Instrum. Exp. Tech. 51 (1) (2008) 1–27.

[8] C. Evain, C. Szwaj, E. Roussel, M. Le Parquier, S. Bielawski, E. Roussel, J. Brubach, L. Manceron, M. Tordeux, M. Labat, et al., High repetition-rate electro-optic sampling: Recent studies using photonic time-stretch, in: Proceedings of the 6th International Beam Instrumentation Conference IBIC2017, 2017, pp. 121–124.

[9] D.V. Karlovets, A.P. Potylitsyn, Diffraction radiation from a finite-conductivity screen, JETP Lett. 90 (2009) 326–331.

[10] A. Curcio, M. Bergamaschi, R. Corsini, W. Farabolini, D. Gamba, L. Garolfi, R. Kieffer, T. Lefevre, S. Mazzoni, K. Fedorov, et al., Noninvasive bunch length measurements exploiting cherenkov diffraction radiation, Phys. Rev. Accel. Beams 23 (2) (2020) 022802.

[11] A. Schlögelhofer, Bunch length measurement studies using cherenkov diffraction radiation, in: Invited talk at Future Circular Collider conference (FCC week) 2022, Paris, 2022.

[12] K. Holldack, M.v. Hartrott, F. Hoeft, O. Neitzke, E. Bauch, M. Wahl, Bunch fill pattern at BESSY monitored by time-correlated single photon counting, in: Advanced Photon Counting Techniques II, vol. 6771, SPIE, 2007, pp. 281–288.

[13] F. Sannibale, M.S. Zolotorev, D. Filippetto, G.V. Stupakov, Absolute bunch length measurements at the ALS by incoherent synchrotron radiation fluctuation analysis, in: 2007 IEEE Particle Accelerator Conference, PAC, IEEE, 2007, pp. 2661–2663.

[14] T. Mitsuhashi, M. Tadano, Measurement of bunch length using intensity interferometry, in: Proc. of the European Particle Accelerator Conference EPAC2002, 2002, p. 1936.

[15] J. Feikes, K. Holldack, P. Kuske, G. Wüstefeld, Sub-picosecond electron bunches in the BESSY storage ring, in: Proceedings of the European Particle Accelerator Conference EPAC2004, 2004, p. 1954.

[16] K. Scheidt, Review of streak cameras for accelerators: features, applications and results, in: Proceedings of the European Particle Accelerator Conference EPAC2000, 2000, pp. 182–186.

[17] A.H. Lumpkin, The next generation of RF FEL (free electron laser) diagnostics: synchroscan and dual-sweep streak camera techniques, Nucl. Instrum. Methods Phys. Res. A 304 (1–3) (1991) 31–36.

[18] L. Torino, Longitudinal and Transverse Beam Diagnostic using Synchrotron Radiation at ALBA (Ph.D. thesis), Università di Pisa, 2017.

[19] M. Koopmans, Two-Dimensional Bunch-Resolved Optical Beam Diagnostics at BESSY II (Ph.D. thesis), Humboldt-Universität zu Berlin, 2022.

[20] M. Ries, et al., Ongoing experimental campaign of pulse-length measurements for different ring conditions in the negative low-alpha mode, 2024, in preparation.

[21] R. Müller, T. Birke, F. Falkenstern, H. Glass, P. Kuske, R.O.A. Schälicke, D. Schüler, K. Holldack, BESSY II supports an extensive suite of timing experiments, in: Proceedings of the 7th Int. Particle Accelerator Conf. IPAC'16, 2016, pp. 2840–2843.

[22] M. Ries, Nonlinear Momentum Compaction and Coherent Synchrotron Radiation at the Metrology Light Source (Ph.D. thesis), Humboldt-Universität zu Berlin, 2014.

[23] G. Wüstefeld, Short bunches in electron storage rings and coherent synchrotron radiation, in: Proceedings of the 11th European Particle Accelerator Conference EPAC2008, 2008, pp. 26–30.

[24] G. Schiwietz, J.-G. Hwang, A. Jankowiak, M. Koopmans, M. Ries, Bunch-resolved diagnostics for a future electron-storage ring, Nucl. Instrum. Methods Phys. Res. A 990 (2021) 164992.

[25] J. Breunlin, Å. Andersson, N. Milas, Á.S. Hernández, V. Schlott, Methods for measuring sub-pm rad vertical emittance at the Swiss Light Source, Nucl. Instrum. Methods Phys. Res. A 803 (2015) 55–64.

[26] Å. Andersson, M. Böge, A. Lüdeke, V. Schlott, A. Streun, Determination of a small vertical electron beam profile and emittance at the Swiss Light Source, Nucl. Instrum. Methods Phys. Res. A 591 (3) (2008) 437–446.

[27] E. Rossa, C. Bovet, L. Disdier, F. Madeline, J. Savioz, Real time measurement of bunch instabilities in LEP in three dimensions using a streak camera, in: Proceedings of the 3rd European Particle Accelerator Conference, Berlin, 1992, pp. 144–146.

[28] E. Rossa, Real time single shot three-dimensional measurement of picosecond photon bunches, in: AIP Conference Proceedings, Vol. 333, American Institute of Physics, 1995, pp. 148–159.

[29] B. Yang, A.H. Lumpkin, K. Harkay, L. Emery, M. Borland, F. Lenkszus, Characterizing transverse beam dynamics at the APS storage ring using a dual-sweep streak camera, in: AIP Conference Proceedings, Vol. 451, AIP Publishing, 1998, pp. 229–236.
[30] B. Yang, Streak camera 101: Visualizing charged-particle beam dynamics, in: AIP Conference Proceedings, Vol. 868, American Institute of Physics, 2006, pp. 124–137.
[31] J.C. Bergstrom, J.M. Vogt, The optical diagnostic beamline at the Canadian light source, Nucl. Instrum. Methods Phys. Res. A 562 (1) (2006) 495–512.
[32] M. Switka, W. Hillert, et al., Preserving information of the three spatial electron beam dimensions in one streak camera measurement, in: Proc. 6th Int. Particle Accelerator Conf. IPAC'15, 2015, pp. 144–146.
[33] The mirror-based entrance-optics A6856 is one of the specific Hamamatsu modifications of our type C10910 FSC.
[34] Selection of Optronis streak-camera accessories, 2024, https://optronis.com/en/products/optoscope-sc-10-systeme/.
[35] P. Baumgärtel, P. Grundmann, T. Zeschke, A. Erko, J. Viefhaus, F. Schäfers, H. Schirmacher, RAY-UI: new features and extensions, in: AIP Conference Proceedings, Vol. 2054, AIP Publishing, 2019, 060034.
[36] K. Kinoshita, M. Ito, Y. Suzuki, Femtosecond streak tube, Rev. Sci. Instrum. 58 (6) (1987) 932–938.
[37] J.D. Jackson, Classical Electrodynamics, Walter de Gruyter, Berlin, New York, 1981.
[38] Data taken from the Hamamatsu test report of our type C10910 FSC.
[39] M. Rösler, Theory of particle-induced kinetic electron emission from simple metals: Comparative studies of different excitation and scattering mechanisms for Al, Mg, and Be, Appl. Phys. A 61 (1995) 595–607.
[40] G. Schiwietz, J.-G. Hwang, M. Koopmans, M. Ries, A. Schälicke, Development of the electron-beam diagnostics for the future BESSY-VSR storage ring, in: Journal of Physics: Conference Series, Vol. 1067, IOP Publishing, 2018, 072005.
[41] T. Urakami, Y. Takiguchi, K. Kinoshita, Y. Tsuchiya, Characterization of photon-counting streak camera, in: High Speed Photography, Videography, and Photonics IV, Vol. 693, SPIE, 1986, pp. 98–104.
[42] K. Kinoshita, Y. Suzuki, Streak tube with microchannel plate, in: 13th Intl Congress on High Speed Photography and Photonics, Vol. 189, SPIE, 1979, pp. 504–507.
[43] Data for various glasses are obtained from the database and evaluation code by M. Polyanskiy, 2023, https://refractiveindex.info/.
[44] Abbe diagram, showing the refractive index vs. its inverse normalized dispersion difference (the Abbe number) for about 100 Schott glasses, 2023, https://www.schott.com/de-de/interaktives-abbe-diagramm.
[45] Basic explanation of the group velocity, 2023, https://en.wikipedia.org/wiki/Group_velocity.